Ab initio relativistic spin-polarized theory of angle-resolved photoemission

M Woods[1], A Ernst[2,3], P Strange[1] and W M Temmerman[2]

[1] Physics Department, Keele University, Keele, Staffordshire ST5 5BG, UK
[2] Daresbury Laboratory, Daresbury, Warrington WA4 4AD, Cheshire, UK
[3] Max Planck Institut für Mikrostrukturphysik, Halle, Germany

Abstract
An *ab initio* real-space fully relativistic spin- and angle-resolved photoemission
theory has been developed. The method is based on density functional theory
and implemented using multiple-scattering theory with a Green's function
calculated using a real-space cluster method. An efficient computer code has
been developed to calculate the spectra. Interpretation of the results reveals
the signatures of relativity in the photoemission spectra, and indicates what
photoemission can tell us about relativistic effects in the band structure. We
illustrate our theory and code by presenting results for transition metal surfaces.

1. Introduction

Density functional theory (DFT) is a highly successful theory of the ground-state electronic
properties of condensed matter. It is now a routine matter to calculate band structures using
the local density approximation (LDA) to DFT. A full knowledge of the electronic structure
is the key to understanding the solid-state properties of a material. Experimentally, the probe
of choice for determining the electronic structure on a band-by-band basis is angle-resolved
photoemission spectroscopy (ARPES) [1]. Photoemission provides a convenient and much-
used probe of the electronic properties [2]. The basis of this spectroscopy is the photoelectric
effect in which the energy of an incident photon is transferred entirely to an electron of the
irradiated material, which may then escape and be detected in an electron spectrometer. In
photoelectron spectroscopy the surface of the sample is irradiated by monochromatic light
of energy $\hbar\omega$ and the kinetic energy of the emitted electrons is measured. Angle-resolved
photoemission determines, apart from the energy, the emission angle of the photoelectrons and
thus measures the external momentum. Finally, in spin- and angle-resolved photoemission the
polarization of the emitted electrons can also be analysed. These observables yield information
about the binding energy E_B, the momentum $\boldsymbol{k}$, and the spin $\boldsymbol{s}$ of the electrons inside the solid.
By proper choice of the angle and polarization of the incident radiation, the analysis of the
electron energy spectrum obtained can be simplified enormously by applying the symmetry

selection rules [3]. In the photoemission process an electron below the Fermi energy E_F initially has energy E_i, and after excitation due to the photon of frequency ω it has an energy $E_i + \hbar\omega$. If the electron was excited to just above the Fermi energy it would not escape from the solid. There is a potential step, or work function Φ, that must be overcome before the electron can escape. Hence the kinetic energy of the electron is written as

$$E_{kin} = \hbar\omega + E_i - \Phi. \tag{1}$$

The availability of a variable photon energy source in the form of synchrotron radiation has transformed angle-resolved photoemission into a practical and versatile tool in physics. In particular it has made possible the mapping of band structures of solid materials. It is particularly useful for investigating the surface properties of materials. If a photon of energy $\hbar\omega$ and given polarization is incident at a given angle to the crystal surface normal n, which defines the z-direction in a system of coordinates, then it is clear that the surface is intrinsic to this experiment. Furthermore, since a number of inelastic collisions impart to the electron a finite mean free path, only a few atomic layers near to the surface can actually contribute to the photocurrent. Durham [1] suggests that the number is closer to ten than one hundred.

Photoelectron spectroscopy probes the ground state of the system by looking at an excited state. Both the excited electron in the bulk final state and the created hole can interact with the other electrons in the solid. These multi-electron effects cause both lifetime broadening and a binding energy shift of the photoemission peaks in the case of screening or fast decay processes. The peak width in photoemission is determined by both the inverse electron lifetime (final-state broadening) and the inverse hole lifetime (initial-state broadening). An example in valence band photoemission is Ni. Due to a high density of states at the Fermi energy in Ni, the emission of a photoelectron can cause the excitation of a second electron into these unoccupied states at the Fermi level leaving a two-hole final state behind.

The need to treat systems relativistically is clear. As is well known, relativistic effects, such as spin–orbit coupling, play a role in the electronic structure of all materials, and this increases dramatically with atomic number. These effects were studied in pure metals by McDonald *et al* [4] and Fasol *et al* [5] and in random alloys by Ginatempo and Staunton [6]. Strange [7] discusses relativistic effects in solids in general. All these calculations have their foundations in relativistic spin-density functional theory, so any calculation that bridges the gap between first-principles energy bands and experimentally measured photoemission spectra is worthwhile.

For pure metals the framework for the required calculations of the photocurrent has already been developed. A quite general theory that includes ferromagnetic order on an equal footing with relativistic effects was put forward by Ackermann and Feder [8]. A theory of energy- and angle-resolved photoemission spectroscopy of non-magnetic crystalline metals on the basis of relativistic quantum mechanics was written down first by Ginatempo *et al* [9]. Here we present a derivation of the theory of relativistic spin-polarized photoemission based on the real-space Green's function method [10]. The real-space multiple-scattering theory offers a fertile field of investigations of systems with arbitrary arrangements of atoms. It also has the advantage of a simple expression for the photocurrent in terms of site-off-diagonal multiple-scattering quantities and the site-dependent matrix elements. This theory implements the real-space theory of Durham [11], within the framework of the one-step model of Pendry [2]. The derivation follows the work, and is formulated analogously to the non-relativistic equation, of Ernst *et al* [12]. This theory is a reformulation of the work of Ebert and Schwitalla [13] and applied to a cluster of atoms rather than an infinite solid. We then present calculations of the relativistic effects in the complex band structure of Ni using magnetic circular dichroism on the perpendicularly magnetized (001) surface. Comparison of spin-resolved photoemission

spectra in the geometrically identical (100) direction (in-plane magnetization) highlights the magnetocrystalline anisotropy; hence conclusions may be drawn about the orientation of the magnetic moment of clusters of atoms and at magnetic surfaces.

2. Theory

A one-electron picture of photoemission can be described by an application of the golden rule for the transition between the initial state $|i\rangle$ and the final state $|f\rangle$. For a single process the first-order golden rule can be written as

$$T = -\frac{2}{\hbar} \sum_f \int \int \psi_f^\dagger(r) H'(r) \operatorname{Im} G^r(r, r'; \epsilon_i) H'^\dagger(r) \psi_f(r') \, \mathrm{d}^3r \, \mathrm{d}^3r' \quad (2)$$

where

$$H'(r) = -ec\boldsymbol{\alpha} \cdot A(r) \quad (3)$$

is the perturbation responsible for the transition and describes the electron–photon interaction. Here $G^r(r, r'; \epsilon_i)$ is the retarded Green's function at energy ϵ, and ψ_f is the so-called time-reversed low-energy electron diffraction (LEED) state given by the Lippmann–Schwinger equation

$$\psi_f(r) = \phi(r) + \int G^r(r, r'; \epsilon) V(r') \phi(r') \, \mathrm{d}r' \quad (4)$$

which describes the final state of the electron. The retarded Green's function $G^r(r, r'; \epsilon_i)$ in equation (2) can be calculated using the powerful technique of multiple-scattering theory. The crystal potential $V(r)$ is the total potential in the one-electron Dirac Hamiltonian taken to consist of an array of non-overlapping muffin-tin potentials representing the lattice of atoms:

$$V(r) = \sum_i v_i(r - R_i) \quad (5)$$

and similarly for the effective magnetic field. Accordingly we write the total potential as a sum over the lattice sites R_i where $v_i(r)$ is a muffin-tin potential at site i. Outside the muffin tins a constant potential is assumed but this restriction is not necessary, and the crystal potential can be taken in the space-filling form as performed by Graß *et al* [14]. This can be partially achieved by placing empty spheres at lattice sites above the surface of the crystal modelled.

An essential feature of this approach is the use of the τ-matrix representation of multiple-scattering theory developed by Györffy and Stott [10] in which the retarded Green's function is defined as

$$G^r(r_i, r_j, \epsilon) = \sum_{\Lambda_1} \sum_{\Lambda_2} Z_{\Lambda_1}(r_i; \epsilon) \tau_{\Lambda_1 \Lambda_2}^{ij}(\epsilon) Z_{\Lambda_2}^\#(r_j; \epsilon) - \sum_\Lambda Z_\Lambda(r_<) J_\Lambda^\#(r_>; \epsilon) \delta_{ij}. \quad (6)$$

The τ-matrix $\tau_{\Lambda'\Lambda''}^{ij}(\epsilon)$ is a site and κm_j decomposition of the total T-matrix at energy ϵ, and the functions $Z_{\Lambda'}(r; \epsilon)$ and $J_{\Lambda'}(r; \epsilon)$ are the regular and irregular solutions of the Kohn–Sham–Dirac equation with the single-site muffin-tin potential $v(r)$. These can be expanded in terms of radial and angular components:

$$Z_{\Lambda'}(r; \epsilon) = \sum_{\kappa''=\kappa', -\kappa'-1} \begin{pmatrix} g_{\kappa''\kappa'}^{m_j'}(r) \chi_{\kappa''}^{m_j'}(\hat{r}) \\ \mathrm{i} f_{\kappa''\kappa'}^{m_j'}(r) \chi_{-\kappa''}^{m_j'}(\hat{r}) \end{pmatrix} \quad (7)$$

and

$$J_\Lambda(r; \epsilon) = \sum_{\kappa'=\kappa, -\kappa-1} \begin{pmatrix} g_{\kappa'\kappa}^{m_j i}(r) \chi_{\kappa'}^{m_j}(\hat{r}) \\ \mathrm{i} f_{\kappa'\kappa}^{m_j i}(r) \chi_{-\kappa'}^{m_j}(\hat{r}) \end{pmatrix}. \quad (8)$$

The # notation in equation (6) is identical to the conjugate transpose for real energies but at imaginary energies one must only take the conjugate transpose of the angular component and not the radial term [15]. The $\chi_\kappa^{m_j}$ are the usual relativistic spin-angular functions [7].

Using equation (6) for the retarded Green's function with $r < r'$ in the Dyson equation (4), the time-reversed LEED state takes the following convenient form:

$$\psi_f(r) = \frac{4\pi}{\sqrt{V}}\left(\frac{W+mc^2}{2W}\right)^{1/2} \sum_{\kappa m_j}(-\mathrm{i})^l C(l\tfrac{1}{2}j; m_j + m_s \ -m_s)Y_l^{m_j-m_s}(-\hat{k})$$
$$\times \sum_j \mathrm{e}^{\mathrm{i}kR_j}\sum_\Lambda \tau_{\Lambda'\Lambda}^{ij*}(\epsilon)\left[\hat{\tau}Z_{\Lambda'}(r;\epsilon)\right] \tag{9}$$

where $C(l\tfrac{1}{2}j; m_j + m_s, -m_s)$ is a Clebsch–Gordan coefficient, $Y_l^{m_j+m_s}(-\hat{k})$ is a complex spherical harmonic, and $\hat{\tau}$ is the time-reversal operator. Equation (9) is the expression for the final state of the electron after photoemission.

Using the scattering path operator representation of the retarded Green's function (6) and equation (9) in (2), the photocurrent can be given as a sum of the inter-site contribution $M_{ij}(\epsilon + \hbar\omega)$, and the intra-site contribution $I_i(\epsilon + \hbar\omega)$:

$$T = \sum_{ij} M_{ij}(\epsilon + \hbar\omega) + \sum_i I_i(\epsilon + \hbar\omega). \tag{10}$$

Taking each in turn, the inter-site term, involving sites i and j, is

$$M_{ij}(\epsilon + \hbar\omega) = \frac{\mathrm{i}}{\hbar}\frac{16\pi^2}{V}\left(\frac{W+mc^2}{2W}\right)$$
$$\times \sum_{\Lambda_1\Lambda_2}(f_{\Lambda_1}^i(\epsilon + \hbar\omega)\tau_{\Lambda_1\Lambda_2}^{ij}(\epsilon)e_{\Lambda_2}^j(\epsilon + \hbar\omega) - d_{\Lambda_1}^i(\epsilon + \hbar\omega)\tau_{\Lambda_1\Lambda_2}^{ij*}(\epsilon)g_{\Lambda_2}^j(\epsilon + \hbar\omega)) \tag{11}$$

which requires a few definitions in order to get it into this form. These are

$$f_{\Lambda_1}^i(\epsilon + \hbar\omega) = \sum_{\Lambda'} U_{\Lambda'}^{im_s}(\epsilon + \hbar\omega)F_{\Lambda'\Lambda_1}^i(\epsilon + \hbar\omega) \tag{12}$$

$$d_{\Lambda_1}^i(\epsilon + \hbar\omega) = \sum_{\Lambda'} U_{\Lambda'}^{im_s}(\epsilon + \hbar\omega)D_{\Lambda'\Lambda_1}^i(\epsilon + \hbar\omega) \tag{13}$$

$$e_{\Lambda_2}^j(\epsilon + \hbar\omega) = \sum_{\Lambda'''} U_{\Lambda'''}^{jm_s*}(\epsilon + \hbar\omega)E_{\Lambda_2\Lambda'''}^j(\epsilon + \hbar\omega) \tag{14}$$

$$g_{\Lambda_2}^j(\epsilon + \hbar\omega) = \sum_{\Lambda'''} U_{\Lambda'''}^{jm_s*}(\epsilon + \hbar\omega)G_{\Lambda_2\Lambda'''}^j(\epsilon + \hbar\omega). \tag{15}$$

Here $F_{\Lambda'\Lambda_1}^i(\epsilon + \hbar\omega)$, $D_{\Lambda'\Lambda_1}^i(\epsilon + \hbar\omega)$, $E_{\Lambda_2\Lambda'''}^j(\epsilon + \hbar\omega)$, and $G_{\Lambda_2\Lambda'''}^j(\epsilon + \hbar\omega)$ are matrix elements:

$$F_{\Lambda'\Lambda_1}^i(\epsilon + \hbar\omega) = \int [\hat{\tau}Z_{\Lambda'}(\epsilon + \hbar\omega, r)]^\dagger H'(r)Z_{\Lambda_1}(\epsilon; r)\,\mathrm{d}r \tag{16}$$

$$D_{\Lambda'\Lambda_1}^i(\epsilon + \hbar\omega) = \int [\hat{\tau}Z_{\Lambda'}(\epsilon + \hbar\omega; r)]^\dagger H'(r)Z_{\Lambda_1}^{\#\dagger}(\epsilon, r)\,\mathrm{d}r \tag{17}$$

$$E_{\Lambda_2\Lambda'''}^i(\epsilon + \hbar\omega) = \int Z_{\Lambda_2}^\#(\epsilon, r)H'^\dagger(r)[\hat{\tau}Z_{\Lambda'''}(\epsilon + \hbar\omega; r)]\,\mathrm{d}r \tag{18}$$

$$G_{\Lambda_2\Lambda'''}^i(\epsilon + \hbar\omega) = \int Z_{\Lambda_2}^\dagger(\epsilon, r)H'^\dagger(r)[\hat{\tau}Z_{\Lambda'''}(\epsilon + \hbar\omega; r)]\,\mathrm{d}r \tag{19}$$

and the $U_\Lambda^{m_s}(\epsilon + \hbar\omega)$ terms contain the geometrical factors

$$U_{\Lambda'}^{im_s*}(\epsilon + \hbar\omega) = \sum_{j'} e^{ikR_{j'}} \sum_\Lambda i^l C(l\tfrac{1}{2}j; m_j + m_s, -m_s) Y_l^{m_j+m_s*}(-\hat{k}) \tau_{\Lambda\Lambda'}^{j'i*}(\epsilon). \tag{20}$$

The intra-site term is

$$I_i(\epsilon + \hbar\omega) = \frac{i}{\hbar} \frac{16\pi^2}{\sqrt{V}} \left(\frac{W + mc^2}{2W}\right) \sum_{\Lambda_1} (a_{\Lambda_1}^i(\epsilon + \hbar\omega) - b_{\Lambda_1}^i(\epsilon + \hbar\omega)) \tag{21}$$

with

$$a_{\Lambda_1}^i(\epsilon + \hbar\omega) = \sum_{\Lambda'\Lambda'''} U_{\Lambda'}^i(\epsilon + \hbar\omega) A_{\Lambda'\Lambda_1\Lambda'''}^i(\epsilon + \hbar\omega) U_{\Lambda'''}^{i*}(\epsilon + \hbar\omega) \tag{22}$$

and

$$b_{\Lambda_1}^i(\epsilon + \hbar\omega) = \sum_{\Lambda'\Lambda'''} U_{\Lambda'}^i(\epsilon + \hbar\omega) B_{\Lambda'\Lambda_1\Lambda'''}^i(\epsilon + \hbar\omega) U_{\Lambda'''}^{i*}(\epsilon + \hbar\omega) \tag{23}$$

where again $A_{\Lambda'\Lambda_1\Lambda'''}^i(\epsilon + \hbar\omega)$ and $B_{\Lambda'\Lambda_1\Lambda'''}^i(\epsilon + \hbar\omega)$ are the matrix elements defined for $r < r'$ as

$$A_{\Lambda'\Lambda_1\Lambda'''}^i = \int\int [\hat{\tau} Z_{\Lambda'}(\epsilon'; r)]^\dagger H'(r) Z_{\Lambda_1}(\epsilon; r) J_{\Lambda_1}^\#(\epsilon; r') H'^\dagger(r') [\hat{\tau} Z_{\Lambda'''}(\epsilon'; r')]\, dr\, dr' \tag{24}$$

and

$$B_{\Lambda'\Lambda_1\Lambda'''}^i = \int\int [\hat{\tau} Z_{\Lambda'}(\epsilon'; r)]^\dagger H'(r) Z_{\Lambda_1}^{\#\dagger}(\epsilon; r) J_{\Lambda_1}^\dagger(\epsilon; r') H'^\dagger(r') [\hat{\tau} Z_{\Lambda'''}(\epsilon'; r')]\, dr\, dr' \tag{25}$$

and for $r > r'$ as

$$A_{\Lambda'\Lambda_1\Lambda'''}^i = \int\int [\hat{\tau} Z_{\Lambda'}(\epsilon'; r)]^\dagger H'(r) J_{\Lambda_1}(\epsilon; r) Z_{\Lambda_1}^\#(\epsilon; r') H'^\dagger(r') [\hat{\tau} Z_{\Lambda'''}(\epsilon'; r')]\, dr\, dr' \tag{26}$$

and

$$B_{\Lambda'\Lambda_1\Lambda'''}^i = \int\int [\hat{\tau} Z_{\Lambda'}(\epsilon'; r)]^\dagger H'(r) J_{\Lambda_1}^{\#\dagger}(\epsilon; r) Z_{\Lambda_1}^\dagger(\epsilon; r') H'^\dagger(r') [\hat{\tau} Z_{\Lambda'''}(\epsilon'; r')]\, dr\, dr' \tag{27}$$

where we have defined $\epsilon' = \epsilon + \hbar\omega$ simply to fit the equations conveniently onto the page.

The separation of the photocurrent equation into two contributing terms is done for convenience only because the intra-atomic term $I_i(\epsilon + \hbar\omega)$ vanishes for real energies and need not be calculated in this case. Thus we have obtained a fully relativistic photocurrent formula which is valid for any atomic arrangement. In essence we need to solve the multiple-scattering problem, that is to find the single-site solution for the t-matrix, and the τ-matrices for low and high energies, which can be done using many well known methods.

One approach for evaluating equations (10), (11), and (21) is the real-space cluster method. In this case the τ-matrix can be obtained by inversion of the KKR matrix:

$$\underline{\tau}(\epsilon) = [\underline{t}^{-1}(\epsilon) - g_{0\, lml'm'}(\epsilon)]^{-1} \tag{28}$$

with the real-space structure constants

$$g_{0\, lml'm'}^{ij}(\epsilon) = -4\pi i q \sum_{l''m''} i^{l-l'+l''} C_{lml'm'}^{l''m''} h_{l''}^{(1)}(q|R_i - R_j|) Y_{l''}^{m''}(\widehat{R_i - R_j}). \tag{29}$$

Here $h_{l''}^{(1)}(q|R_i - R_j|)$ is a spherical Hankel function of the first kind, $\underline{t}(\epsilon)$ is the single-site t-matrix, and $C_{lml'm'}^{l''m''}$ is a Gaunt coefficient.

3. Practical aspects of the calculations

The real-space KKR method is very simple and can be applied for any arrangement of scatterers in the cluster. The accuracy of this approach depends on the convergence of the τ-matrix. This convergence is determined by the size of the KKR matrix that can be inverted. To model a surface accurately we find that it is necessary to take into account in excess of 100 atoms, because of the long-range behaviour of the structure constants (29). Figure 1 shows the convergence of the angle-resolved photocurrent for incident light of $\hbar\omega = 44.0$ eV as a function of the size of cluster. This calculation was performed with broadening in the energy of 0.01 Ryd. What is evident is that the main features of the experiment [16] are revealed by a relatively small cluster of 45 atoms but the photocurrent is not close to convergence until we have a cluster size of 87 atoms. The photocurrent for the cluster of 87 atoms is closer to that of the experiment but in this case the KKR matrix is large, approximately 2800×2800, and needs 1.5 hours of CPU time on a DEC Alpha 500 Series for the inversion of one energy point [17]. However, with the inversion completed, the photocurrent emitted at all other angles can be calculated without any further matrix inversion. The calculation for new directions is related to that for the first by a series of simple trigonometric factors.
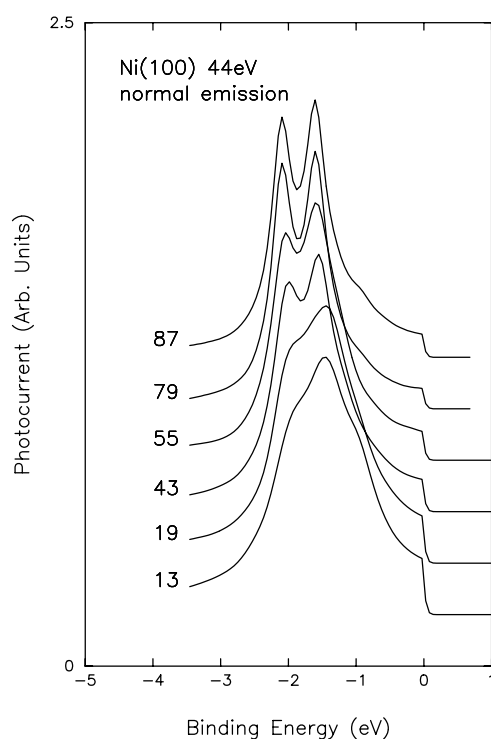

Figure 1. Calculated photoemission spectra with 44 eV incident photons and normal emission for Ni(100) from different sized FCC configured clusters of atoms.

Lifetime and instrumental broadening of the photocurrent spectra can be simulated by evaluating it with a small imaginary component added to the energy. This is illustrated in figure 2(a) where photoemission spectra for the Ni(100) surface are presented for several values of the imaginary component of the energy. The rapid smoothing as a function of the imaginary part of the energy is clearly visible.
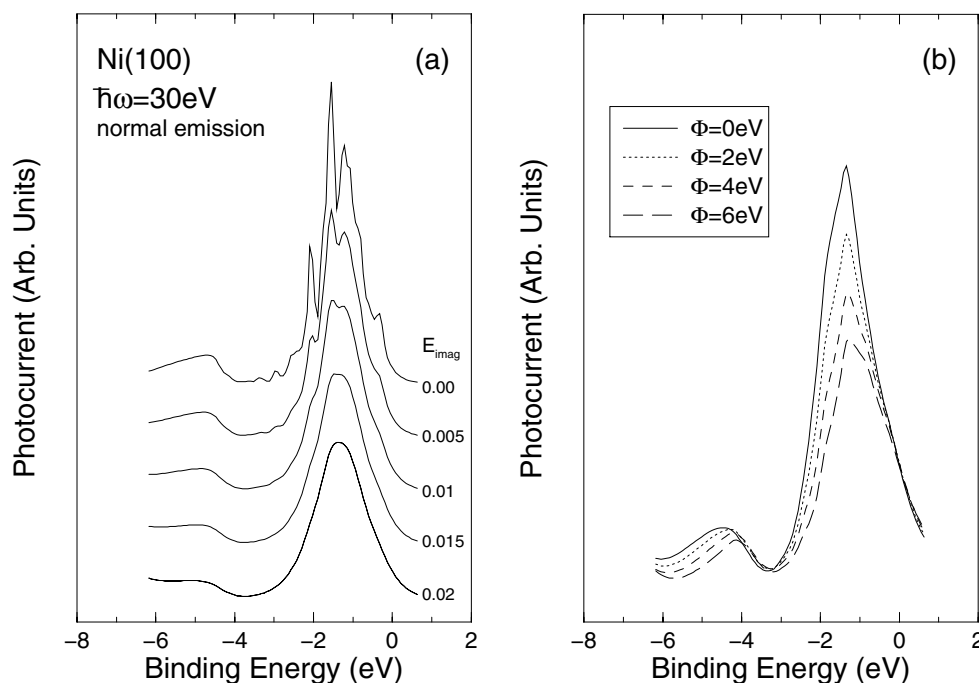
Figure 2. Photoemission spectrum of Ni(100) ($N_{atoms} = 55$). (a) Photoemission calculated with different imaginary parts in the final-state energies. (b) Photoemission calculated with different work functions.

The application of the work function adds a surface barrier to the material which prevents the electrons from simply escaping into the vacuum. The work function decreases the kinetic energy of the electrons and decreases the number of electrons that can escape from the material for a given incident energy photon. This effect is shown in figure 2(b) where calculations have been performed for a variety of work functions. Work functions for Fe, Co, and Ni are widely published and are in the region of 4.3–4.4 eV.

To set up the cluster we take a central site and a number of nearest-neighbour shells. We then remove the appropriate sites to create the desired surface, so, for example, to create a (001) surface all lattice sites with z-component less than zero are removed. A potential and an effective spin-only field are then placed at all the remaining lattice sites and the Kohn–Sham–Dirac equation is solved with the field in the z-direction, and the t-matrices may be set up in the usual way [18]. It is possible to rotate the direction of the moment using standard rotation matrix methods.

In principle we may place any potential and field at any site in the cluster. However, for the illustrative purposes of this paper we have used a potential and field calculated self-consistently for the bulk material at all lattice sites. While such an approach is unlikely to yield numerical agreement with experiment it should be sufficient to enable us to correlate features in the photoemission spectrum with the electronic structure. Furthermore, such an approach has the advantage that it enables us to separate geometrical effects due to the presence of a surface on the photoemission spectrum from effects due to the modification of the potential due to the presence of the surface. Thus this is a good example of where first-principles theory of materials can really enhance our understanding and interpretation of experiment.

Of course, many extensive checks can be made on the code to ensure that it gives reliable results. It may be taken for granted that these checks were made. However, we would like to point out one test we made that proved to be very instructive and strict. With the magnetic moment in the (001) direction the photocurrents in the (010) and (100) directions from equivalent clusters must be identical. If the moment is rotated to the (100) direction, say, the photocurrent in the (010) and (001) directions must take on the same values again. We must also get identical answers if the photocurrent is calculated with the magnetic moment and the incident photon direction parallel, whichever of the equivalent crystallographic axes we choose for the calculation. Needless to say, our code does satisfy all the required symmetry conditions.

The selection rules were worked out for the electric dipole and electric quadrupole/magnetic dipole transitions. The latter were found to be insignificant and were not included in the calculations presented here. In applications to f-electron materials it may be necessary to look at this again.

All matrix elements should be calculated in the unit cell of the crystal. It is possible to restrict the integrals to the muffin-tin spheres by using the acceleration formula [9]. This is done by transforming the operators so they all contain either the effective potential or field. As these quantities are zero outside the muffin tin there can be no contribution to the matrix elements from this region. Hence one only needs to do the calculations within the muffin-tin sphere. We have worked out the acceleration formula for the relativistic case with a spin-only magnetic field in the z-direction and for a general matrix element we find

$$\langle \psi_{\kappa m_j}(E + \hbar\omega) | ec\tilde{\alpha} \cdot \boldsymbol{a}_\lambda | \psi_{\kappa' m'_j}(E) \rangle$$

$$= \frac{2iec^2}{\omega(2E + \hbar\omega)} \langle \psi_{\kappa m_j}(E + \hbar\omega) | a_\lambda (\nabla V(\boldsymbol{r}) - \mu_B \nabla B_z(\boldsymbol{r})\tilde{\beta}) | \psi_{\kappa' m'_j}(E) \rangle$$

$$+ \frac{2ec}{(2E + \hbar\omega)} \langle \psi_{\kappa m_j}(E + \hbar\omega) | \tilde{\alpha} \left(a_\lambda V(\boldsymbol{r}) - \frac{i\hbar e}{m} B_\lambda \tilde{\beta} \right) | \psi_{\kappa' m'_j}(E) \rangle \qquad (30)$$

where

$$\boldsymbol{B}_\lambda = \hat{\boldsymbol{i}} a_y B_z(\boldsymbol{r}) - \hat{\boldsymbol{j}} a_x B_z(\boldsymbol{r}). \qquad (31)$$

Clearly these equations satisfy the conditions given above and therefore only have to be evaluated within the muffin-tin sphere. However, they are rather complicated and so we have decided to calculate the matrix elements using the original form of the operator and make the Wigner–Seitz approximation to facilitate the integration.

4. Calculations for nickel metal

Nickel is an interesting transition metal to study with spin- and angle-resolved photoemission because the electronic structure part of the calculation causes the theoretical results to differ drastically from experimental ones [19]. The measured exchange splitting is one half of the magnitude of the calculated splitting and the d bandwidth is approximately 30% smaller than the calculated width [20]. Typical exchange splittings in Ni are between 200 and 300 meV, which is close to the intrinsic linewidth of the peaks in the photoemission spectra determined by the lifetime of the observed transitions. Only close to the Fermi energy is the lifetime of the excited states long enough to result in sufficiently small linewidths to resolve separate peaks. Spin-resolved photoemission experiments have determined exchange splittings in Ni and have shown that the exchange splitting Δ_{ex} depends strongly on the energy, the wavevector, and the symmetry of the band [21]. Magnetic circular dichroism (MCD) further enhances the resolution of photoemission experiments and can be used to identify points of hybridization between

bands of different spin occupancy and different orbital symmetry where the expectation of spin polarization is low. By performing calculations of band structures and photoemission spectra using the same potential and structural parameters we can correlate one with the other. For the above reasons we have performed calculations with photon energies in the range of 11 to 44 eV and binding energies close to the Fermi level. We have calculated the valence band MCD to compare with spin-resolved photoemission spectra to gain deeper insight into the details of the d band structure of Ni(001).

4.1. Electronic structure of Ni(001)

Figure 3 shows the theoretical band structure for nickel. The approach used to calculate the bands was by finding the zeros of the KKR determinant as given by equation (28) for an infinite solid. This approach allows us to treat spin polarization and all relativistic effects on the same footing, and therefore describes the hybridization of the ('non-relativistic') minority and majority bands due to spin–orbit coupling in a rigorous way [22]. The presence of a magnetization generally reduces the symmetry of a semi-infinite solid. However, when it is perpendicular to the crystal surface, the surface normal remains a rotation axis, and the electronic states can be classified according to irreducible double-group representations of the non-magnetic case [23]. In panel (a) the bands are displayed with differently dashed and dotted lines according to their double-group symmetry, as labelled in the figure. Panel (b) shows the same band structure displaying the spin of the bands. Thick (thin) lines indicate bands that are predominantly majority (minority) spin. Note that in a relativistic calculation it is possible for bands to have different spin character in different regions of the Brillouin zone. For comparison panel (c) shows the non-relativistic spin-polarized band structure and panel (d) shows the relativistic non-magnetic band structure. All four band structures were calculated with the same potential.

Before it is possible to deduce information about the spin–orbit and exchange-split valence band structure, the relation between the calculated photoemission spectra and the fully relativistic band structure, calculated with the same parameters, has to be provided. The model of direct transitions serves to correlate specific details of the photoemission spectra with details of the relativistic band structure. In the present geometry, circularly polarized light at normal incidence dictates that only bands with Δ_5 spatial symmetry, and any bands involved in hybridization with them, contribute to the photoemission signal. To facilitate the correlation with the photoemission spectra of figure 4, sections of the final-state band of Δ_1 symmetry, shifted down by the photon energies used in the calculation, are depicted in figure 3(a) by weak solid vertical lines. The crossings between these lines and the bands mark the energetic positions of the features in the photocurrent spectra.

4.2. Magnetic circular dichroism in Ni

Right and left circularly polarized incident radiation provokes transitions from different states. This dichroic signal dramatically enhances the resolution of experiments and, via the selection rules, is of considerable use in plotting precise relativistic band structure. Panel (a) of figure 4 shows photoemission spectra for different photon energies from 11 up to 30 eV. Spectra for positive light helicity (LCP) are represented by solid lines and those for negative helicity (RCP) are represented by dotted lines. The calculation is performed on a cluster of 87 atoms cut along the (001) axis and with broadening in the energy of 0.01 Ryd. Since we are in normal emission, the selection rules dictate that with right circularly polarized photons, only bands with $\Delta_{6^+}^5$ and $\Delta_{7^-}^5$ symmetry will contribute to the signal. Excitation by left circularly polarized incident
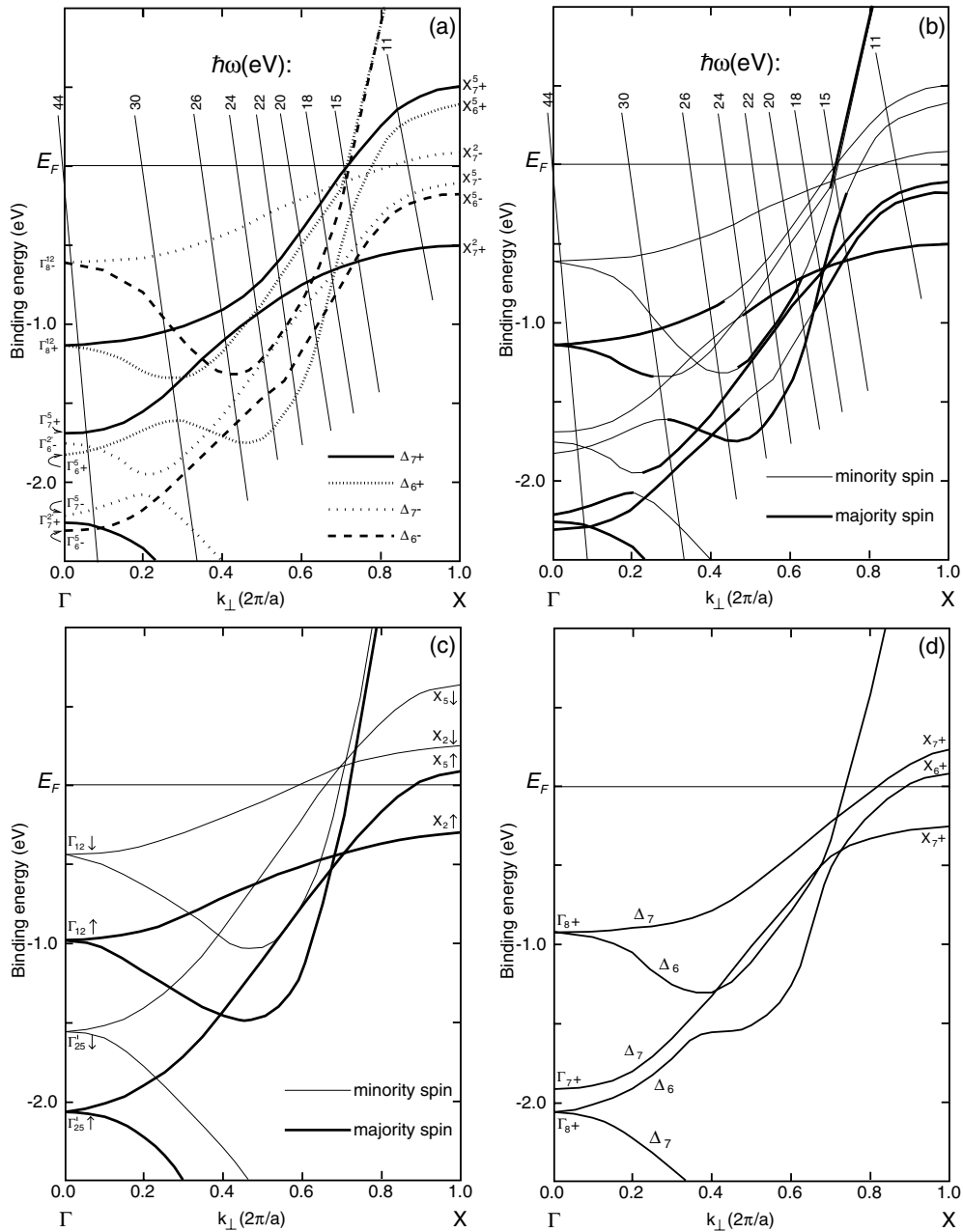
Figure 3. Symmetry-resolved real valence band structure of Ni(001), calculated with the same parameters as the photoemission spectra. (a) Bands with Δ_{7^+}, Δ_{6^+}, Δ_{7^-}, and Δ_{6^-} double-group symmetry are distinguished as labelled in the figure. The thin solid lines are sections of the final-state band, shifted down by the photon energy indicated at the respective line. (b) As in (a), but with the bands distinguished by their minority- (majority-) spin expectation value shown by thin (thick) solid lines. For comparison panel (c) is the same as (b) but calculated non-relativistically and panel (d) is the same as (b) but calculated with the spin polarization set equal to zero.
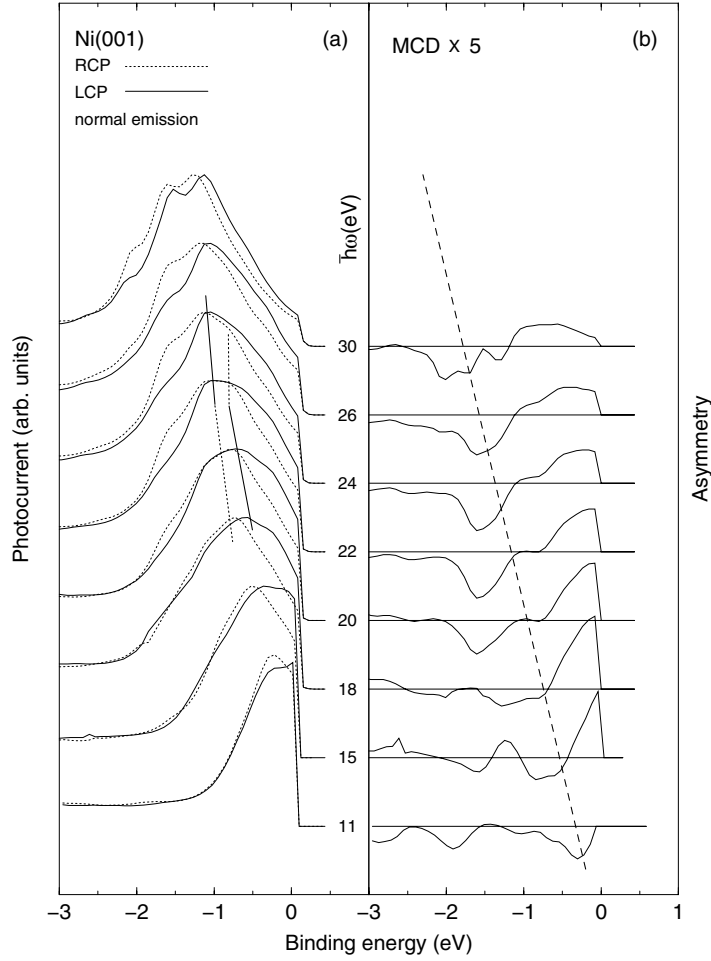
Figure 4. Series of photoemission spectra for different photon energies $\hbar\omega$. Shown are the spectra for right (solid lines) and left (dotted lines) circularly polarized photons incident normal to the Ni(001) surface plane. The vertical lines indicate the occurrence of a hybridization region as explained in the text. (b) Series of asymmetry spectra for panel (a). The vertical dotted line indicates the dispersion of the prominent negative peak.

photons means that only Δ_{6-}^{5} and Δ_{7+}^{5} symmetry bands make up the signal. The structure in the energy distributions between 0 and -2 eV binding energy can be clearly seen, by comparison with figure 3(a), to be due to the d bands of Ni.

To illustrate the dichroism more clearly, figure 4(b) shows the normalized asymmetry, defined as

$$A(\hbar\omega; E_B) = \frac{I^+(\hbar\omega; E_B) - I^-(\hbar\omega; E_B)}{I^+(\hbar\omega; E_B) + I^-(\hbar\omega; E_B)} \tag{32}$$

for the spectra of figure 4(a). Several characteristics of the photon energy series can be seen in the asymmetries. With increasing photon energy the asymmetry is reduced. This is due to the decrease of the lifetime of the initial states moving away from E_F. At all photon energies there is one pronounced negative feature which disperses towards higher binding energies with increasing photon energy. The near-vertical line in panel (b) indicates the dispersion of

this feature. At 11 eV photon energy the negative peak is located just below the Fermi edge whereas at 30 eV it exhibits a binding energy of -1.8 eV. In the case with no hybridization of the bands with Δ_5 spatial symmetry, the situation is like the one shown in figure 3(a), but more symmetric. Only the four bands of Δ_5 spatial symmetry contribute to the photoemission signal in that case, and the negative peak in the MCD gives the energetic position of the centre of the bands with Δ_5 spatial symmetry.

The valence band structure of Ni(001) (figure 3(a)) shows avoided crossings where bands with different single-group symmetry (in the non-relativistic band structure), but identical double-group symmetry, hybridize. These avoided crossings occur simply because the spin–orbit coupling changes the band symmetry [16]. When the bands hybridize and change their spatial symmetry, they may also change their spin occupancy, and this is seen clearly in figure 3(b).

In the energy range from -2.5 eV up to the Fermi level (0 eV) in figure 3(a), Δ_{6^+} initial states show spin–orbit-induced band gaps at $k_\perp = 0.3(2\pi/a)$ and at $k_\perp = 0.7(2\pi/a)$. These are evident in the negative-helicity spectra (dotted lines) of figure 4(a) at 30 and 15 eV photon energies respectively. The Δ_{6^-} initial states show such gaps at $k_\perp = 0.45(2\pi/a)$ and $k_\perp = 0.6(2\pi/a)$. For the occupied bands with Δ_{7^+} and Δ_{7^-} symmetry, there is only one gap each at $k_\perp = 0.5(2\pi/a)$ and $k_\perp = 0.2(2\pi/a)$ respectively.

Let us consider first the hybridization of bands with Δ_{7^+} symmetry. This hybridization gap is the result of an avoided crossing of bands with Δ_2 and Δ_5 spatial symmetry. The steeper $\Delta_{7^+}^5$ band of minority-spin character changes symmetry (and spin occupancy) with the flatter $\Delta_{7^+}^2$ majority band. This hybridization occurs in the photoemission spectra of 22 and 24 eV photon energy. The vertical lines in figure 4(a) indicate the hybridization region. They mark the corresponding peaks in the photoemission intensity for left circularly polarized incident photons. The continuous lines show the positions of the bands containing $\Delta_{7^+}^5$ symmetry, and fade out into dotted lines where the $\Delta_{7^+}^2$ symmetry character in these bands predominates.

The next hybridization region that we will discuss is the hybridization between the bands of Δ_{6^-} symmetry. One of these bands is the sp-like minority band with Δ_1 spatial symmetry which starts at $\Gamma_{8^-}^{12}$ and reaches a minimum in binding energy at $k_\perp = 0.4(2\pi/a)$. It hybridizes with a band of $\Delta_{6^-}^5$ symmetry producing two hybridization gaps at $k_\perp = 0.45(2\pi/a)$ and $k_\perp = 0.6(2\pi/a)$. Between these gaps the bands are separated by less than 0.3 eV. Therefore they have a low expectation value of spin polarization and exhibit a considerable mixing of spatial symmetry. Both bands contain a significant portion of $\Delta_{6^-}^5$ symmetry and should therefore appear in both left circularly polarized minority- and majority-spin spectra.

The other hybridization regions of initial bands containing Δ_5 character which have not yet been discussed are bands of Δ_{7^-} and Δ_{6^+} double-group symmetry. The former hybridization gap occurs above the 30 eV excitation energy and hence is not visible in this study. Transitions for Δ_{6^+} bands appear in the right circularly polarized spectra at 15 and 30 eV photon energies of figure 4(a). In the 30 eV spectra the two peaks at -1.25 and -1.6 eV mark the hybridization point at $k_\perp = 0.3(2\pi/a)$. Between 30 and 15 eV the spin-down $\Delta_{6^+}^5$ band has swapped spatial symmetry and spin character with the spin-up $\Delta_{6^+}^1$ band.

Figure 5 shows spin-resolved photoemission spectra attained with 44 eV photons incident normal to the Ni(001) and Ni(001) surfaces. Incident radiation of this frequency probes the Brillouin zone close to Γ and right and left circularly polarized incident photons will produce an asymmetry that is of use in determining the spin–orbit and magnetic anisotropy in local regions of k-space. The top part of the figure decomposes the total photocurrent (solid line) attained with left circularly polarized incident radiation into minority- (dashed lines) and majority- (dotted lines) spin contributions. Clearly the peak at -1.5 eV binding energy identifies transitions from the $\Delta_{7^+}^5$ band with predominant minority-spin character. The peak
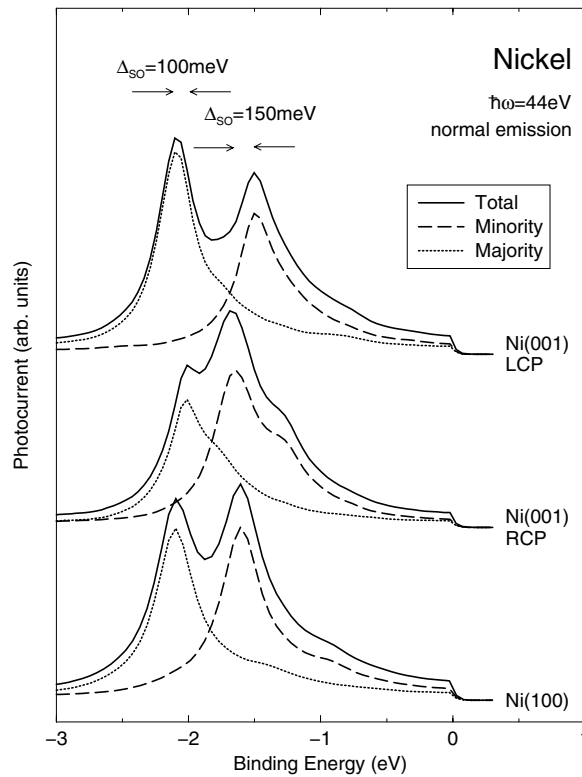
Figure 5. Photocurrent from nickel with 44 eV incident photons. The full line shows the total photocurrent; the dashed (dotted) line shows the minority- (majority-) spin photocurrent. Top: the photocurrent found from Ni(001) (perpendicular magnetization) with left circularly polarized incident photons. Middle: the photocurrent found from Ni(001) (perpendicular magnetization) with right circularly polarized incident photons. Note the offset between the peaks for the two polarizations. Bottom: the photocurrent at the Ni(100) surface (parallel magnetization) where there is no dichroism.

at -2.1 eV marks transitions from the majority Δ_{6-}^5 band. The middle section shows similar spectra attained with right circularly polarized incident radiation. This time the features mark transitions from Δ_{6+}^5 bands, at -1.65 eV, and Δ_{7+}^5 bands, at -2.0 eV. The energy differences between the peaks measure the spin–orbit coupling as 150 and 100 meV respectively. It is clear then that fully relativistic photoemission is, in principle, capable of yielding a great deal of information about the details of the band structure of materials beyond what may be discovered from interpretation within a non-relativistic theory. The lower part of figure 5 is for photons incident on the (100) surface with in-plane magnetization. The spin splitting is still clearly visible, but there is no dichroism in this case.

5. Calculations for iron metal

As a bulk system, iron has a complicated phase diagram, but at room temperature it is found in the BCC phase with a magnetic moment of $2.21\mu_B$. However, FCC iron is metastable as a thin film on FCC substrates such as Cu(001). In contrast to the BCC phase, which is ferromagnetic over a wide range of lattice spacings, FCC Fe assumes different magnetic

configurations ranging from a high-spin ferromagnetic and a low-spin antiferromagnetic to a non-magnetic phase over a very narrow range of lattice parameters [24]. This moment/volume instability is interesting from the physical point of view and technologically in Invar alloys.

An increasingly improved picture of magnetism in thin magnetic films of FCC iron is being built up. There seem to be three distinct phases. In the first region between zero and four monolayers (ML) on Cu, ferromagnetic alignment is observed. A sharp drop in the magnetic signal is observed between 4 and 10 ML and films above this thickness display a gradual increase in their magnetic moment again [25, 26]. The non-vanishing small magnetic signal of the second phase is attributed to a ferromagnetically ordered surface layer with large magnetic moments and a paramagnetic interior of the film at room temperature. A recent spectrographic investigation by Gubanka *et al* [27] confirms a surface magnetic moment in the second phase. In the following section we use spin-resolved photoemission and magnetic circular dichroism to see what they can tell us about magnetic order in a small FCC cluster of 55 Fe(001) atoms. We have placed a charge- and spin-self-consistent muffin-tin potential for Fe, with a lattice constant of 5.27 au, at each atomic site.

Figure 6 shows the spin-resolved band structure for FCC magnetic iron along two perpendicular directions in the Brillouin zone. Panel (a) shows the band structure in the (001) direction with perpendicular magnetism—hence the double-point-group labelling of the bands. Panel (b) shows the (100) direction where the moment is oriented in the plane and double-group symmetry labelling is no longer possible. The vertical solid lines are sections of the final-state band shifted down by the two energies used in the calculation. At the Γ point the binding energies are identical in each graph of course. At this point the band structure yields values
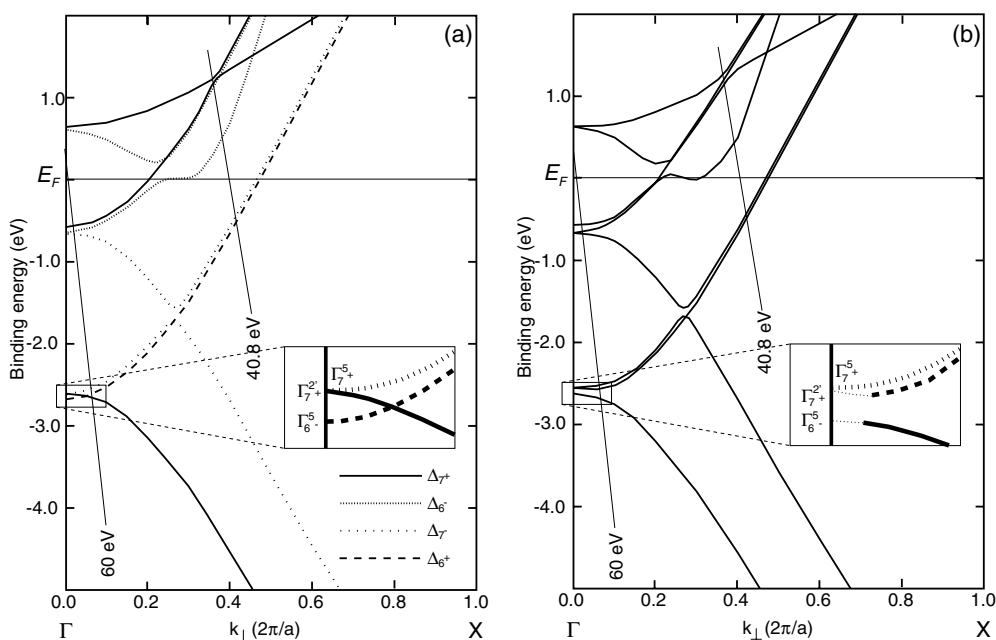

Figure 6. (a) Symmetry-resolved valence band structure, in the (001) direction, of FCC Fe calculated with the same parameters as the photoemission spectra. Bands with the Δ_{7+}, Δ_{6+}, Δ_{7-}, Δ_{6-} double-group symmetry are distinguished as labelled in the figure. The thin solid lines show sections of the final-state band, shifted down by the photon energy indicated on the respective lines. (b) As (a) but calculated for the (100) direction.

for the exchange splitting of 2.1 eV and the crystal-field splitting between the majority bands is 3.3 eV. The spin–orbit splitting at Γ between the minority Δ_{7-}^5 and the Δ_{6-}^5 bands can be seen to be 64 meV. A value of 62 meV is visible between the Δ_{7-}^5 and the Δ_{6+}^5 bands. The inset boxes in figures 6(a) and 6(b) not only show up the spin–orbit splitting at Γ, but also exhibit the differences in band structure as we move along the Δ axis in directions that are crystallographically equivalent, but magnetically distinct. For convenience of discussion the bands in the (100) inset of panel (b) are displayed with the same double-group symmetry as in (a), but the reader should note that this is not strictly true and the bands can only be said to display similar (not identical) symmetry away from Γ. As can be seen in panel (a), the selection rules allow the $\Delta_{7+}^{2'}$ and $\Delta_{6-}^{5'}$ bands to cross at $k_\perp(2\pi/a) \simeq 0.1$. In panel (b) for the (100) direction, this crossing is not allowed. Although at Γ the bands may be labelled identically to the (001) bands, hybridization of the bands due to spin–orbit coupling causes an immediate change of symmetry of the bands. For this reason the bands are displayed with thin dotted lines close to Γ, and with the same double-group symmetry labelling above $k_\perp(2\pi/a) \simeq 0.1$, where the bands behave similarly to the (001) bands. This anisotropy is due to the interaction between the spin–orbit coupling and the magnetization direction.

Figure 7 shows the spin-resolved photoemission spectra calculated assuming that 60 eV photons are incident normal to the Fe(001) and Fe(100) surfaces. Incident radiation of this energy probes the bands close to Γ. Panel (a) decomposes the total photocurrent (solid line) obtained with right circularly polarized incident radiation into minority- (dashed line) and majority- (dotted line) spin contributions. Clearly the peak at -0.65 eV binding energy identifies transitions from the Δ_{6+}^5 band with predominantly minority-spin character. The peak at -2.5 eV marks transitions from the Δ_{7-}^5 band. Panel (b) shows similar spectra obtained with left circularly polarized radiation. This time the features mark transitions from Δ_{6-}^5 at -2.6 eV and Δ_{7+}^5 at -0.55 eV. The total emission curves from panels (a) and (b) are reproduced in panel (c) and the spin–orbit splitting of 90 meV can be clearly seen.

Magnetic anisotropy can be examined in photoemission calculations. We can compare spectra probing close to Γ in both the (001) and (100) geometries. The lack of dichroism on the (100) surface is not a problem because the two Δ_5 spatial symmetry bands, that contribute exclusively to the majority-spin signal, are degenerate at Γ. The difference between the peak positions produced by left circularly polarized incident photons probing close to Γ in the two symmetry directions can measure the local k-resolved magnetocrystalline energy differences due to perpendicular and in-plane magnetization. Comparison of the peaks in panels (c) and (d) yields an energy difference of 50 meV. Similarly, at around -0.5 eV there is an energy difference of 50 meV due to the minority-spin band with approximate Δ_{6-}^5 symmetry shifting upwards and swapping places with the Δ_{7-}^5-like band at Γ.

Figure 8 shows the spin-resolved photoemission spectra obtained with 40.8 eV photons incident normal to the Fe(001) and Fe(100) surfaces and thus probes the Brillouin zone at roughly $k_\perp = 0.4$. Panel (a) superimposes minority- and majority-spin spectra obtained with right and left circularly polarized radiation as described in the caption. Clearly the main feature is predominantly majority spin in character and locates the bands with Δ_{6+}^5 and Δ_{7-}^5 symmetry which have dispersed upwards in binding energy towards the Fermi level. The energy difference between the majority-spin peaks at -0.5 eV gives a value for the spin–orbit splitting of 60 meV at $k_\perp(2\pi/a) = 0.4$. Comparison with the peak marked with an arrow in panel (b), due to the same transition in the (100) direction, yields a local anisotropy energy difference of 100 meV. The computation of many k-resolved energy differences across the whole Brillouin zone with different spin arrangements is required to tell us the easy axis of magnetizations. However, the present calculation illustrates the fact that, in principle, photoemission measurements should be able to give us information about magnetocrystalline anisotropy energies and tell us the
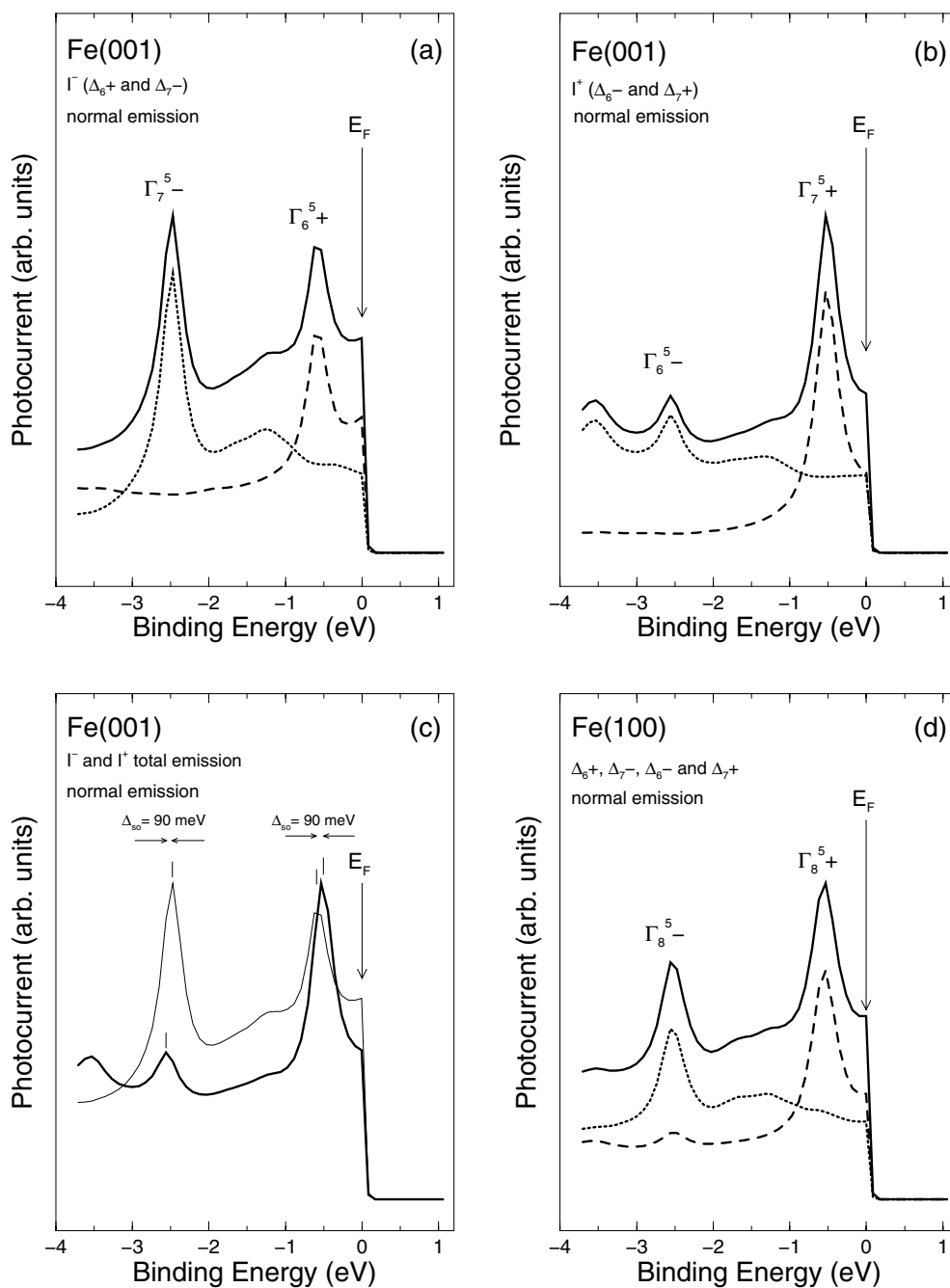
Figure 7. Spin-resolved photoemission spectra obtained with 60 eV photons incident normal to the Fe(001) (perpendicular magnetization) and Fe(100) (in-plane magnetization) surfaces. Solid lines represent total emission and dashed (dotted) lines represent contributions from minority- (majority-) spin channels. (a) Right circularly polarized incident photons at the (001) surface. (b) Left circularly polarized incident photons at the (001) surface. (c) The asymmetry between the total spectra of panels (a) and (b) yields the spin–orbit splitting. (d) Spin-resolved photoemission from the Fe(100) surface.
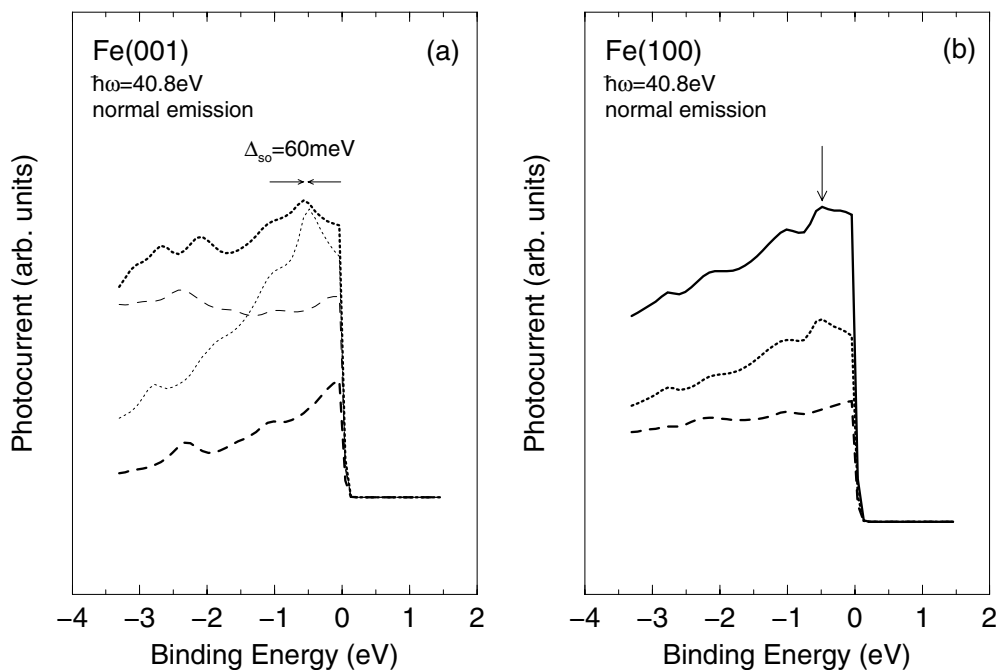
Figure 8. Spin-resolved normal-photoemission spectra obtained with 40.8 eV photons incident normal to the Fe(001) (perpendicular magnetization) and Fe(100) (in-plane magnetization) surfaces. Dashed (dotted) lines represent contributions from the minority- (majority-) spin channels. (a) Right (left) circularly polarized incident photons are represented by thick (thin) lines respectively. (b) The solid line represents total emission.

positions in the Brillouin zone where the dominant contributions to the magnetocrystalline energy occur.

6. Summary

In this paper we have reported on the development of a real-space fully relativistic spin- and angle-resolved photoemission code in the independent-particle approximation. The method underlying this development is formulated in terms of multiple-scattering theory with the real-space representation of the Green's function. The multiple-scattering part in the photocurrent formula is separated from the angle-dependent part, leading to a substantial simplification of the photocurrent calculations. The photocurrent formula is general and can be easily adapted to the symmetry of the problem through a transformation of the multiple-scattering part. To evaluate the multiple-scattering part of the photocurrent formula one needs to obtain the single-site solution and the τ-matrices for low and high energies. These preliminary calculations have shown good agreement with experiment and other theoretical calculations. Incident photon-energy-resolved results are a direct probe of the band structure and comparison of results obtained with incident photons of different helicity yields the spin–orbit splitting. Probing with photoemission close to Γ in two perpendicular directions of the Brillouin zone reveals local k-resolved magnetic anisotropies which yield important information about the direction of the magnetic moment.

Acknowledgments

References

[1] Durham P J 1981 *J. Phys. F: Met. Phys.* **11** 2475
[2] Pendry J B 1976 *Surf. Sci.* **57** 679
[3] Klasges R 1998 Magnetism and quantum-size effects of thin fcc films *Thesis* University of Koln
[4] McDonald A H, Daams J M, Vosko S H and Koelling D D 1981 *Phys. Rev.* B **23** 6377
[5] Fasol G, Christensen N E and Cardona M 1988 *Phys. Rev.* B **38** 1806
[6] Ginatempo B and Staunton J B 1988 *J. Phys. F: Met. Phys.* **18** 1827
[7] Strange P 1998 *Relativistic Quantum Mechanics* (Cambridge: Cambridge University Press)
[8] Ackermann B and Feder R 1985 *J. Phys. C: Solid State Phys.* **18** 1093
[9] Ginatempo B, Durham P J and Györffy B L 1989 *J. Phys.: Condens. Matter* **1** 6483
[10] Györffy B L and Stott M J 1973 *Band Structure Spectroscopy of Metals and Alloys (NATO)* ed D J Fabian and
      L M Watson (New York: Academic) p 385
[11] Durham P J 1984 *The Electronic Structure of Complex Systems (NATO ASI Series B: Physics, vol 113)* ed
      P Phariseau and W M Temmerman (New York: Plenum) p 709
[12] Ernst A, Temmerman W M, Szotek Z, Woods M and Durham P J 1998 *Phil. Mag.* B **78** 503
[13] Ebert H and Schwitalla J 1997 *Phys. Rev.* B **55** 3100
[14] Graß M, Braun J and Borstel G 1993 *Phys. Rev.* B **47** 15 487
[15] Tamura E 1992 *Phys. Rev.* B **45** 3271
[16] Kuch W, Zharnikov M, Dittschar A, Meinel K, Schneider C M, Kirschner J, Henk J and Feder R 1995 *Phys.
      Rev.* B **53** 11 621
[17] *Harwell Subroutine Library* 1997 AEA Technology, Harwell Laboratory, Oxfordshire, UK
[18] Strange P, Staunton J B and Gyorffy B L 1984 *J. Phys. C: Solid State Phys.* **17** 3355
[19] Himpsel F J, Knapp J A and Eastman D E 1979 *Phys. Rev.* B **19** 2919
[20] Eberhardt W and Plummer E W 1980 *Phys. Rev.* B **21** 3245
[21] Raue R, Hopster H and Claudberg R 1983 *Phys. Rev. Lett.* **50** 1623
[22] Schneider C M, Schuster P, Hammond M, Ebert H, Noffke J and Kirschner J 1991 *J. Phys.: Condens. Matter* **3**
      4349
[23] Fanelsa A, Kisker E, Henk J and Feder R 1996 *Phys. Rev.* B **54** 2922
[24] Moruzzi V L, Marcus P M and Kluber J 1989 *Phys. Rev.* B **39** 6957
[25] Thomassen J, May F, Feldmann B, Wuttig M and Ibach H 1992 *Phys. Rev. Lett.* **69** 3831
[26] Li Dongqi, Freitag M, Pearson J, Qui Z Q and Bader S D 1994 *Phys. Rev. Lett.* **72** 3112
[27] Gubanka B, Donath M and Passek F 1996 *J. Magn. Magn. Mater.* **161** L11